

Reentrant phases in electron-doped EuFe_2As_2 : spin glass and superconductivity

A. Baumgartner,¹ D. Neubauer,¹ S. Zapf,¹ A. V. Pronin,¹ W. H. Jiao,² G. H. Cao,^{2,3} and M. Dressel¹

¹*Physikalisches Institut, Universität Stuttgart, Pfaffenwaldring 57, 70550 Stuttgart, Germany*

²*Department of Physics, Zhejiang University, Hangzhou 310027, China*

³*Collaborative Innovation Center of Advanced Microstructures, Nanjing 210093, China*

(Dated: September 22, 2018)

We report evidence for a reentrant spin glass phase in electron-doped EuFe_2As_2 single crystals and first traces of the superconductivity re-entrance in optics. In the close-to-optimal doped $\text{Eu}(\text{Fe}_{0.91}\text{Ir}_{0.09})_2\text{As}_2$ and $\text{Eu}(\text{Fe}_{0.93}\text{Rh}_{0.07})_2\text{As}_2$ samples two magnetic transitions are observed below the superconducting critical temperature $T_c \approx 21$ K: the canted A -type antiferromagnetic order of the Eu^{2+} ions sets in around 17 K; the spin glass behavior occurs another 2 K lower in temperature. In addition, strong evidence for an additional transition is found far below the spin glass temperature. Our extensive optical and magnetic investigations provide new insight into the interplay of local magnetism and superconductivity in these systems and elucidate the effect of the spin-glass phase on the reentrant superconducting state.

PACS numbers: 74.70.Xa, 74.25.Gz, 74.25.Ha, 75.50.Lk

I. INTRODUCTION

Quite some time passed since in 2008 Hosono *et al.* discovered superconductivity in fluorine-doped LaFeAsO with a T_c of 26 K [1] and by now a large variety of different iron-based superconductors are found and studied [2]. Soon it was realized that in pnictides the interplay of magnetism and superconductivity is crucial for the understanding; the spin-density-wave phase has to be suppressed in order to develop the superconducting phase. Eu-based iron pnictides provide an even more interesting playground, as they allow to study the influence of strongly magnetic Eu^{2+} ions on the superconducting state [3].

The parent compound EuFe_2As_2 develops not only the antiferromagnetic order of the itinerant iron electrons that is typical for iron pnictides ($T_{\text{SDW}} \approx 190$ K); at low temperatures, an additional magnetic order of the local rare earth moments sets in ($T_N \approx 20$ K) [4]. This local magnetism is strong enough for a giant, indirect spin-lattice coupling that allows a structural detwinning of these compounds by small magnetic fields [5]. Nevertheless, superconductivity can be induced on the same temperature scale by chemical substitution or mechanical pressure. This leads to the emergence of interesting phenomena such as spin-glass behavior, reentrant superconductivity and probably spontaneous vortices.

In principle, the reentrant superconductivity is caused by a competition between superconductivity and magnetism. Such unusual behavior of resistivity was first predicted for superconductors exhibiting the Kondo effect by Müller-Hartmann *et al.* [6], but several rare earth compounds also show such a resistivity behavior [7]. In Eu-doped compounds, external magnetic fields affect the appearance of this feature [8–10]. Up to now it is not fully understood why some compositions exhibit reentrant superconductivity and others not.

Here, Eu-based 122 compounds with electron doping are investigated. Thereby, optical, dc and ac magneti-

zation, and dc resistivity measurements are performed. From our study we conclude that reentrant superconductivity is widely present in electron-doped Eu-122 compounds. We can reveal important information on the intermediate regime, $T_{c,0} < T < T_{c,\text{on}}$, where the reentrant spin-glass phase affects superconductivity until complete phase coherence is reached.

II. EXPERIMENTAL DETAILS

The single crystals used for this study were grown by the self-flux method [11, 12] and characterized by x-ray, dc transport and susceptibility measurements. Optical investigations are performed by normal-incidence reflection measurements in the frequency range between $\nu = \omega/(2\pi c) = 12$ and $10\,000\text{ cm}^{-1}$. For the far-infrared range a Fourier-transform spectrometer Bruker IFS 113 v was utilized; the mid-infrared and near infrared data were taken by a Bruker VERTEX 80v. In the far-infrared range *in-situ* gold evaporation technique allows us to measure at very low frequencies. For mid- and near-infrared range an attached Bruker Hyperion 1000 microscope provides optimal results by using a small focus area on the sample. Temperature and field-dependent magnetization data are obtained in three different ways by employing a Quantum Design ac SQUID (superconducting quantum interference device). First, the sample is cooled down without a magnetic field applied and the data are recorded during warming up (zero-field cooled, ZFC). The second way is to measure upon cooling with a field applied (field-cooled cooling curve FCC). The third procedure records the magnetization while warming up, after the sample was cooled down with the magnetic field present (field-cooled heating curve, FCH). The temperature-dependent dc resistivity is measured with the standard four-point probe technique.

In the following we focus on two electron-doped EuFe_2As_2 compounds, one with 7% iron replaced by

rhodium and one with 9% iridium. Our magnetization measurements clearly identify the Eu^{2+} ordering at $T_N \approx 17$ K [4, 13]; in addition all compounds show strong evidence of the reentrant spin-glass state, like it was reported for isovalent substituted $\text{EuFe}_2(\text{As}_{1-x}\text{P}_x)_2$ [14]. This immediately tells us that the spin glass phase is also present in electron-doped compounds and infers that the appearance of the reentrant spin glass phase is important for the formation of the superconducting state. Interestingly, while $\text{Eu}(\text{Fe}_{0.93}\text{Rh}_{0.07})_2\text{As}_2$ and $\text{Eu}(\text{Fe}_{0.91}\text{Rh}_{0.09})_2\text{As}_2$ [10] exhibits reentrant superconductivity, no signs of it are found in $\text{Eu}(\text{Fe}_{0.91}\text{Ir}_{0.09})_2\text{As}_2$. From the infrared results at temperatures below the onset of the superconducting state $T_{c,\text{on}}$, we find distinct differences in the low-frequency optical behavior for the samples with and without reentrant superconductivity.

Besides of that, both samples show an untypical feature in the imaginary part of the magnetic susceptibility χ''_{ac} at very low temperatures. The origin of this feature could be either due to vortex dynamics or attributed to a ferromagnetic transition regarding to the results obtained in Ru-doped samples [15]. This would be consistent with recent publications of neutron diffraction measurements report indications of a ferromagnetic state in c -direction for Co- [16], Ir- [17, 18] and P-doped [19] samples; however they cannot rule out a small canting of the spins which is enough to form a spin glass in the ab -plane. Hence it is reasonable to have a closer look at all features from the results out of the magnetization measurements.

III. TRANSPORT PROPERTIES

Figure 1 displays the temperature-dependence of the in-plane resistivity ρ_{ab} for both alloys, $\text{Eu}(\text{Fe}_{0.91}\text{Ir}_{0.09})_2\text{As}_2$ and $\text{Eu}(\text{Fe}_{0.93}\text{Rh}_{0.07})_2\text{As}_2$. The corresponding residual resistivity ratios (RRR) are $\text{RRR}_{\text{Ir}} = \rho(300\text{ K})/\rho(22\text{ K}) = 2.56$ and $\text{RRR}_{\text{Rh}} = 2.24$, respectively. These values are comparable to those reported for other Ir- and Rh-doped samples [10, 18, 20] and confirm the high quality of our crystals.

In case of $\text{Eu}(\text{Fe}_{0.91}\text{Ir}_{0.09})_2\text{As}_2$, the normal state resistivity depends linearly on T , which is typical for unconventional superconductors close to optimal doping level ($x = 0.12$) [20]. Such a behavior is often ascribed to the vicinity of a quantum critical point [21], but could be also explained by spin fluctuations [22]. In contrast, the resistivity of $\text{Eu}(\text{Fe}_{0.93}\text{Rh}_{0.07})_2\text{As}_2$ depends quadratically on temperature between 25 and 90 K, indicating Fermi liquid behavior. Therefore, this sample is probably slightly under- or overdoped. It is interesting to recall the behavior of BaFe_2As_2 doped with Co and Ni, where a similar distinction was observed [23]. There it was concluded that two electronic subsystems are present with one following a T^2 behavior in $\rho(T)$ up to elevated temperatures, indicating a hidden Fermi-liquid behavior. The superconducting state evolves out of this Fermi-liquid state.

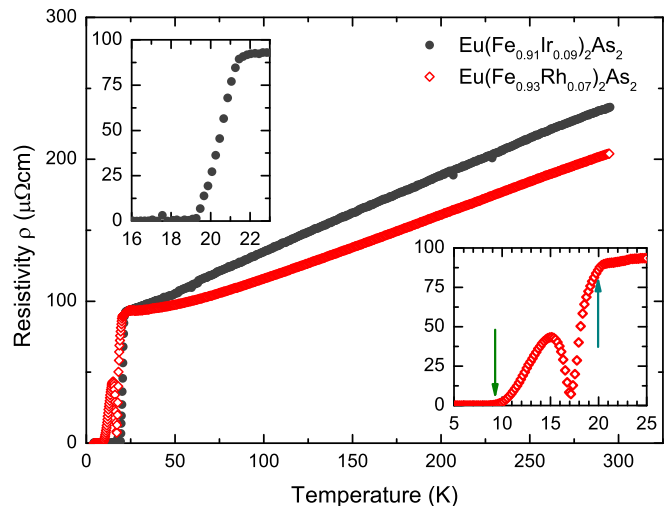


FIG. 1. Temperature-dependent in-plane resistivity of $\text{Eu}(\text{Fe}_{0.91}\text{Ir}_{0.09})_2\text{As}_2$ (black circles) and $\text{Eu}(\text{Fe}_{0.93}\text{Rh}_{0.07})_2\text{As}_2$ (red diamonds); the insets highlight the superconducting transition. While for Ir-doping, $\rho_{ab}(T)$ is linear in T for the normal state and shows a sharp superconducting transition, the Rh doped sample displays a quadratic temperature dependence and a resistivity re-entrance in the vicinity of the europium magnetic ordering at T_N .

Let us now turn to the superconducting state by looking at the insets of Fig. 1. For the optimally doped Ir sample, a sharp superconducting transition takes place between $T_{c,\text{on}} \approx 21$ K and $T_{c,0} \approx 18.9$ K. In contrast, $\text{Eu}(\text{Fe}_{0.93}\text{Rh}_{0.07})_2\text{As}_2$ exhibits a clear resistivity re-entrance: superconductivity sets in at $T_{c,\text{on}} \approx 19.6$ K. However, the resistivity does not directly drop to zero; it goes through a local minimum around $T \approx 17$ K, rises again to a maximum around $T \approx 15$ K and reaches zero only at $T_{c,0} = 9.1$ K. Although reentrant superconductivity for Eu-doped compounds was reported previously, most studies considered the effect of an external magnetic fields on this feature [8, 9]. It is not yet fully understood why the reentrant behavior manifest itself in some compositions, while not detected in others. However, when $T_c \approx T_N$ or $T_N > T_c$, in general reentrant superconductivity behavior is observed [24]. This is also the reason why for samples near optimal doping, where $T_c \gg T_N$, reentrant superconductivity is typically not present.

IV. OPTICAL PROPERTIES

A. Normal state

1. $\text{Eu}(\text{Fe}_{0.91}\text{Ir}_{0.09})_2\text{As}_2$

In Figure 2(a) we plot the optical reflectivity of the optimally doped Ir sample for selected temperatures. As typical for iron pnictides of the 122 family, no clear plasma edge can be detected [4, 25]. In order to max-

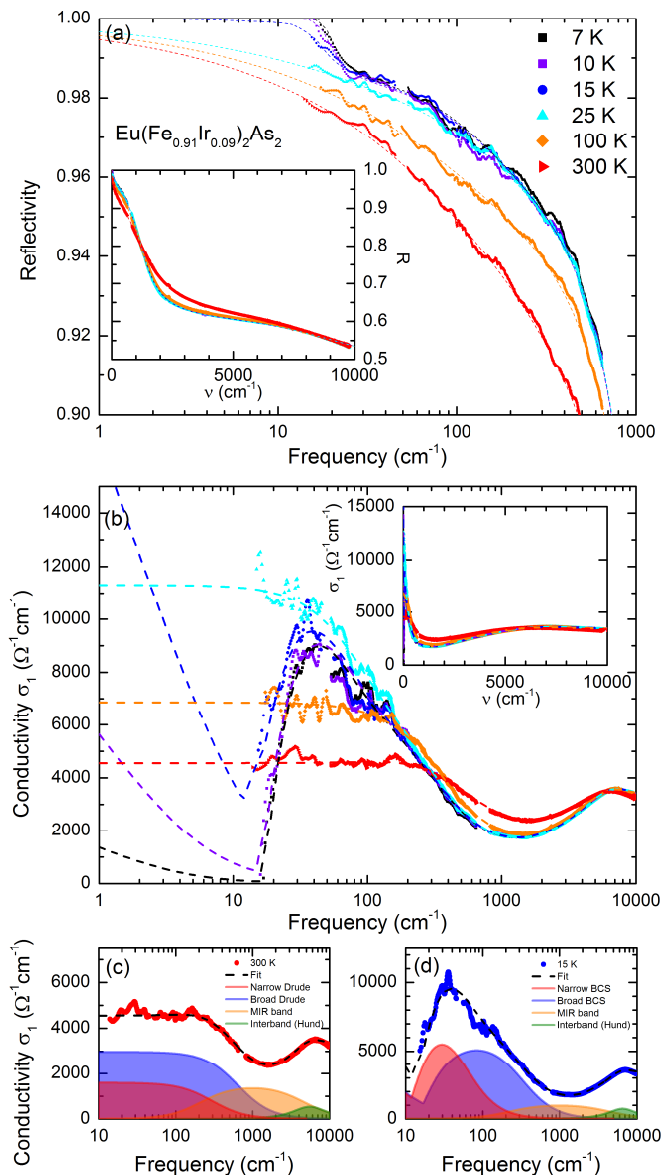


FIG. 2. (a) Optical reflectivity and (b-d) corresponding conductivity of $\text{Eu}(\text{Fe}_{0.91}\text{Ir}_{0.09})_2\text{As}_2$ single crystals plotted for selected temperatures as indicated by different colors. The solid lines correspond to measured data, the dashed lines refer to the fits. The data are replotted on a linear scale in the insets. (a) Below $T = 25$ K, the low-frequency reflectivity shows a pronounced upturn towards unity around $\nu = 10$ to 20 cm^{-1} , giving evidence for the opening of the superconducting energy gaps. (b) Correspondingly, for $T < T_c \approx 21$ K the optical conductivity $\sigma_1(\omega)$ drops towards low frequencies. Moreover, in the normal state spectral weight is transferred from around 1000 cm^{-1} to higher energies as the temperature is reduced. (c) In the metallic state ($T = 300$ K), the fits consist of two Drude terms (blue and red), one mid-infrared Lorentzian (orange) and one temperature-dependent Lorentzian (magenta). Note that several Lorentzians above $10\,000$ cm^{-1} are not shown here. (d) Below T_c , the two Drude contributions are replaced by two BCS terms with two distinct energy gaps, describing the superconducting state, as exemplarily shown for $T = 15$ K. The narrow Drude exhibits the smaller gap.

imize the quality of our fits, reflectivity and optical conductivity are described simultaneously, because the complex components are linked by the Kramers-Kronig relations. Following our previous approach [23, 26], the normal state behavior is decomposed into two Drude components (one narrow, one broad), two mid-infrared Lorentzians, and Lorentzians located at high energies, as illustrated in Fig. 2(c). Since the latter ones are located out of the measured energy range, they are considered temperature-independent to avoid any artificial spectral weight transfer. The spectral weight of a certain conductivity term, SW^{term} , measures how many charge carriers N contribute; it is calculated from the optical conductivity via [27]

$$\text{SW}^{\text{term}} = \int_0^\infty \sigma_1^{\text{term}}(\omega) d\omega = \frac{(\omega_p^{\text{term}})^2}{8} = \frac{\pi N e^2}{2m} \quad (1)$$

Here $\sigma_1^{\text{term}}(\omega)$ is the real part of the conductivity in dependence of frequency $\omega = 2\pi\nu$; the plasma frequency of this term is indicated by ω_p^{term} , e is the elementary charge and m the mass of a charge carriers. Similarly, the spectral weight can be calculated for the total optical spectrum. Here, it is interesting consider the spectral weight as a function of the upper integration limit – the cut-off frequency ω_c :

$$\text{SW}(\omega_c) = \int_{0+}^{\omega_c} \sigma_1(\omega) d\omega \quad , \quad (2)$$

where $\sigma_1(\omega)$ is the real part of the (total) optical conductivity, and the lower integration limit $0+$ emphasizes that in the superconducting state we do not include the zero-frequency δ -function. While calculating the total spectral weight hereafter, we always use $\sigma_1(\omega)$ obtained from the fits.

For each component of the fit, figure 3(a) presents the spectral weight as a function of T . The spectral weight of the narrow Drude component, often linked to the electron bands, has the smallest contribution and stays constant with temperature. This implies that no charge carriers are redistributed to other components. The same holds for the broad Drude term, which possesses a nearly three times larger spectral weight. This ratio is surprising, on the first glance, since the broad Drude component is commonly linked to hole bands, but the sample under investigation is electron-doped. Therefore we should consider other possible interpretation of the two terms based on coherent and incoherent carriers [28].

Already in the conductivity data displayed in Fig. 2(b) it becomes obvious that with decreasing temperature the mid-infrared band loses spectral weight to higher energies. Indeed, this transfer takes place up to surprisingly high energies, as can be best seen from Fig. 3(b-c), which present the spectral weight as a function of cut-off frequency ω_c [see Eq. (2)]. As typical for iron pnictides of the 122-family, the spectral weight (down to $T = 25$ K) is not fully recovered at $10\,000$ cm^{-1} [25, 29], with a discrepancy of $\delta = 3.8\%$ remaining. Such a high-energy

spectral-weight transfer can be ascribed to Hund's rule coupling [30]. In this case, free electrons become polarized by localized carriers and thus do not contribute to the response of itinerant carriers anymore, resulting in a spectral-weight transfer of one Drude component to higher energies. As we have demonstrated for the isovalent substituted $\text{EuFe}_2(\text{As}_{1-x}\text{P}_x)_2$ [25], however, a fit of equal quality can also be obtained by the present approach. Here the scattering rate of the broad Drude term is not artificially high. The mid-infrared band corresponds to contributions by incoherent electrons that – as T decreases – get even more localized by Hund's rule coupling.

2. $\text{Eu}(\text{Fe}_{0.93}\text{Rh}_{0.07})_2\text{As}_2$

Figure 4 depicts the frequency- and temperature-dependent optical reflectivity and conductivity for the Rh-doped sample. In the normal state the overall behavior is very similar to the Ir-substituted crystal. Accordingly, we use the same approach to fit the data, leading to comparable results concerning the spectral weight transfer (see Fig. 5). Again, the spectral weight is not fully recovered up to $10\,000\text{ cm}^{-1}$, with a remaining discrepancy of $\delta = 4\%$.

It is interesting to note the pronounced phonon at 146 cm^{-1} , most obvious in Fig. 4(c)(d). EuFe_2As_2 crystallizes in the tetragonal structure of space group $I4/mmm$ (No.139). Torgashev calculated phonon modes at the Γ -point [31] and obtained two E_u vibrations, which are infrared-active for $E \parallel x, y$. The one at

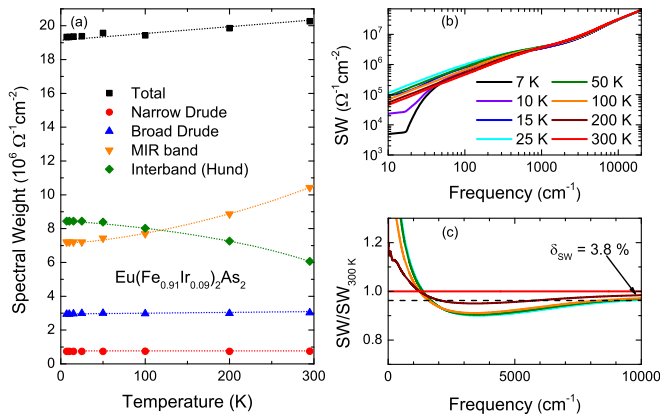


FIG. 3. (a) Temperature- and (b-c) frequency-dependent spectral weight of $\text{Eu}(\text{Fe}_{0.91}\text{Ir}_{0.09})_2\text{As}_2$; dashed lines are guides to the eye. (a) By fitting the spectra with Drude components with moderate scattering rates, the Drude contributions possess constant SW with temperature, and SW is transferred from the MIR band to higher energies. (b) At $T < T_c$, SW at low frequencies is transferred into the delta peak at $\nu = 0\text{ cm}^{-1}$. (c) The normalized curves to 300 K reveal that even at $10\,000\text{ cm}^{-1}$, the spectral weight is not fully recovered with a discrepancy of $\delta_{\text{SW}} = 3.8\%$.

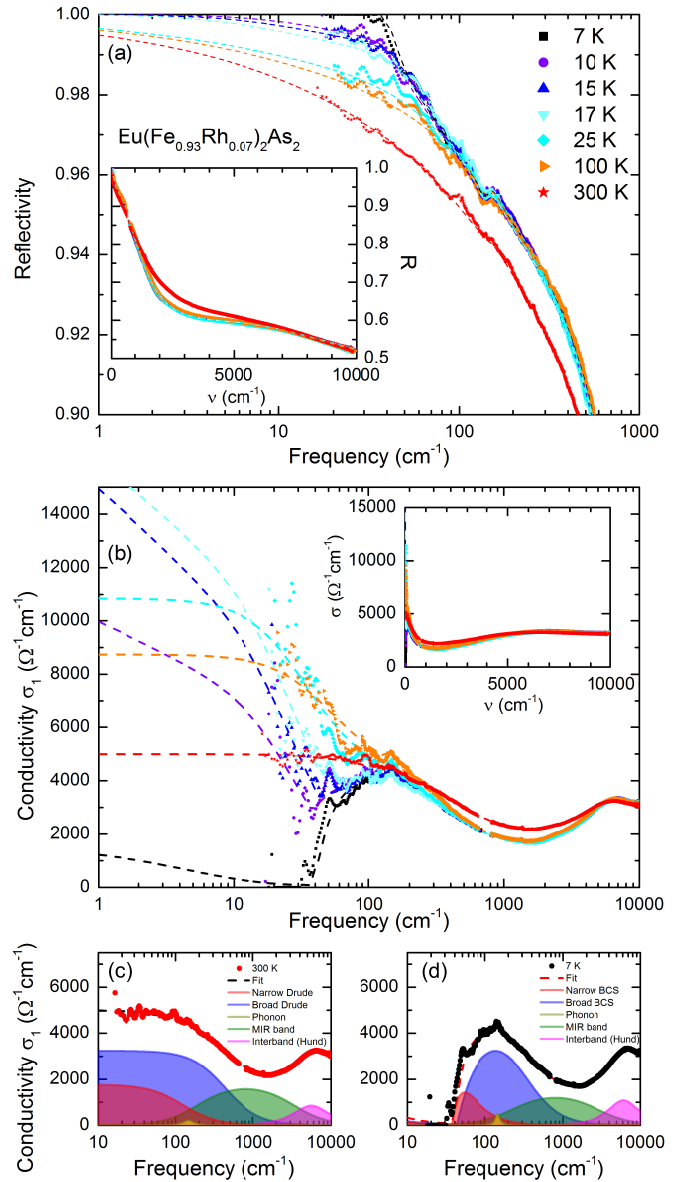


FIG. 4. Temperature-dependent (a) reflectivity and (b-d) optical conductivity of $\text{Eu}(\text{Fe}_{0.93}\text{Rh}_{0.07})_2\text{As}_2$ at selected temperatures. The solid lines denote measurement data, the dashed lines fits and model calculations. (a) Below $T = 25\text{ K}$, the low-frequency reflectivity shows an upturn, but only at 7 K it reaches unity, as typically expected for the superconducting state. (b) Upon entering the superconducting phase, $\sigma_1(\omega)$ drops for frequencies below 100 cm^{-1} , but increases again below 60 cm^{-1} . Moreover, in the normal state, spectral weight is transferred from around 1000 cm^{-1} to much higher energies. The inset presents the optical conductivity on a linear scale. (c) For the normal state ($T = 300\text{ K}$), the fits consist of two Drude terms (blue and red), one phonon (yellow), one mid-infrared Lorentzian (green) and one temperature-dependent Lorentzian (magenta). Note that several Lorentzians above $10\,000\text{ cm}^{-1}$ are not shown here. (d) Below T_c , the two Drude contributions are replaced by two BCS terms, describing the superconducting state, as shown for $T = 7\text{ K}$, as an example.

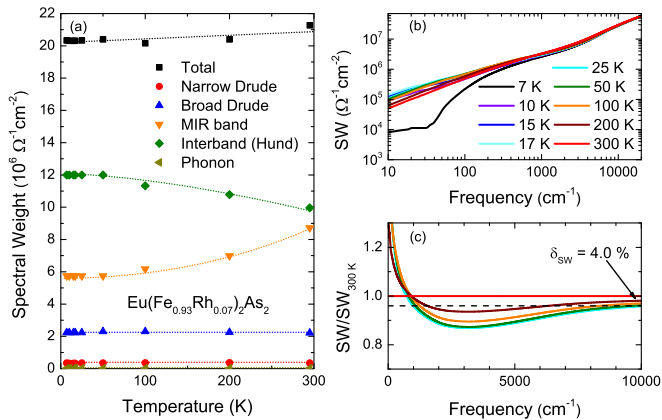


FIG. 5. (a) Temperature- and (b-c) frequency-dependent spectral weight of $\text{Eu}(\text{Fe}_{0.93}\text{Rh}_{0.07})_2\text{As}_2$; dashed lines are guides to the eye. (a) By fitting the spectra by Drude components with moderate scattering rates, these contributions possess constant spectral weight with temperature, and spectral weight is transferred from the mid-infrared band to higher energies. (b) In the superconducting state at $T = 7$ K, spectral weight at low frequencies is transferred into the δ -peak at zero frequency. (c) The curves normalized to the spectral weight at $T = 300$ K reveal that even at $10\,000\text{ cm}^{-1}$, the spectral weight is not fully recovered with a discrepancy of $\delta_{\text{sw}} = 4\%$.

$\nu_0 = 260\text{ cm}^{-1}$ is frequently observed in infrared experiments [4, 25] and also seen in related 122 iron pnictides [32]. By completely substituting Rh for Fe, this E_u -mode should shift by a factor of $\sqrt{m_{\text{Fe}}/m_{\text{Rh}}} \approx \sqrt{1/2}$ and is expected around 180 cm^{-1} ; significantly higher than the observed feature. Thus we believe that we do observe the second E_u -vibration, which is predicted between $\nu = 130\text{ cm}^{-1}$ and 140 cm^{-1} and has not been reported so far. The doping by Rh probably causes slight structural distortions and changes in the electron concentration leading to an enhanced intensity compared to the parent compound.

B. Superconducting state

At $T_{c,\text{on}} \approx 21\text{ K}$ and $T_{c,\text{on}} \approx 19.6\text{ K}$, respectively, superconductivity sets in for the Ir and Rh-doped EuFe_2As_2 crystals, as depicted in Fig. 1. While in the metallic phase both compounds exhibit rather similar optical properties, their behavior in the superconducting state is distinctively different and shall be discussed in full detail in the following.

1. $\text{Eu}(\text{Fe}_{0.91}\text{Ir}_{0.09})_2\text{As}_2$

For the Ir-doped sample we find a clear upturn in reflectivity around 24 cm^{-1} towards unity; the common hallmark of a superconductor with a complete energy gap

at the Fermi surface [27, 33]. In order to describe the electrodynamic behavior below T_c , the two Drude terms are replaced by two BCS contributions [Fig. 2(d)], following the extended Mattis-Bardeen equations [26, 34]. We assume that both contributions remain independent and simply add up. Since we are close to the limit what can be measured by gold-evaporation technique, we restrain from applying more advanced models [35]. As demonstrated in Fig. 3(b), the spectral weight is significantly reduced for $T < T_c$ and transferred to the δ -peak at $\nu = 0\text{ cm}^{-1}$. From the BCS fit of the optical data, the temperature-dependent gaps are extracted and displayed in Fig. 6(a). As expected, both energy gaps start to open simultaneously around 20 K, increase with decreasing T , and basically follow the BCS temperature dependence. The zero-temperature extrapolation yields $2\Delta_1 = 15.7\text{ cm}^{-1}$ and $2\Delta_2 = 19.1\text{ cm}^{-1}$. These absolute values are about a factor of 2.5 to 3 smaller than one would expect from weak-coupling mean-field theory with a $T_c \approx 20\text{ K}$; and also smaller than reported for other iron-based superconductors of the 122 family [2, 36]. It is interesting to compare our findings with one on P-substituted EuFe_2As_2 compounds where no gap was recognized in the optical response, because the samples are clean-limit superconductors [37].

Recently, the coexistence of clean- and dirty-limit superconductivity was proposed to account for the optical properties of LiFeAs [38]. This approach might also be relevant for $\text{Eu}(\text{Fe}_{0.91}\text{Ir}_{0.09})_2\text{As}_2$, as we do observe a clear signature of a small gap but there could be another gap present at higher frequencies. The gap feature is not detected in optical conductivity simply because its position is above the characteristic scattering rates, i.e. the clean-limit situation is realized for this larger gap. By applying these considerations we could explain that the gap observed is three times below the BCS value [39].

2. $\text{Eu}(\text{Fe}_{0.93}\text{Rh}_{0.07})_2\text{As}_2$

The Rh-doped crystals do not only exhibit pronounced reentrant superconductivity in the dc resistivity, as demonstrated in Fig. 1, but also distinct optical properties for $T < T_c$. In a close inspection of the frequency-dependent reflectivity, plotted in Fig. 4(a), clear fingerprints of the re-entrance phase can be resolved below 40 cm^{-1} . At $T = T_{c,\text{on}}$, the onset of superconductivity, the low-frequency reflectivity rises strongly; for instance, the changes between 25 K and 17 K are much bigger than the one observed between 100 K and 25 K. In principle this behavior is typical for a superconducting transition, however, the reflectivity does not shoot up to unity immediately. Only at $T = 7\text{ K}$, i.e. below the zero-resistance temperature $T_{c,0}$, the reflectivity $R(\omega) = 1$ is finally reached. A similar observation is made on the spectral-weight transfer to the zero-frequency peak that can only be observed at the lowest temperature.

The temperature and frequency behavior of the opti-

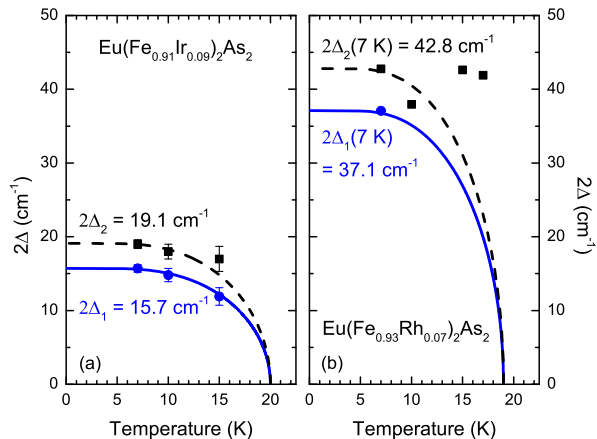


FIG. 6. BCS fits of the two superconductivity gaps for (a) $\text{Eu}(\text{Fe}_{0.91}\text{Ir}_{0.09})_2\text{As}_2$ and (b) $\text{Eu}(\text{Fe}_{0.93}\text{Rh}_{0.07})_2\text{As}_2$. (a) For Ir-doping the energy gaps increase with decreasing temperature below T_c and can be described well by the BCS theory. Note, however, that the ratio $2\Delta/k_B T_c$ falls far below the mean-field value of 3.5. (b) For Rh doped samples larger gaps are observed; however, no temperature dependence can be extracted reliably.

cal conductivity displayed in Fig. 4(b) basically leads to similar conclusions. Only the curves below $T = 25$ K exhibit a drop similar to the Ir-analogue, but then $\sigma_1(\omega)$ increases again for decreasing frequencies due to a strong in-gap absorption. Since there are no explicit models for the frequency-dependence of a re-entrance superconductor, we follow the procedure described above and fit the data by replacing the Drude with a BCS term as the superconducting state is entered. While the larger gap around 42 cm^{-1} is present already below $T \approx 18$ K, it does not change much as T is lowered. Only at $T = 7$ K the narrow term exhibits an energy gap, with 37.1 cm^{-1} ; see Fig. 6(b).

Similar temperature-independent optical gaps – i.e. gap-related features seen in optical experiments – were previously reported in $\text{Ba}(\text{Fe}_{0.92}\text{Co}_{0.08})_2\text{As}_2$ single crystals [40] and $\text{LaFeAsO}_{1-x}\text{F}_x$ thin films [41].

Up to now, the origin of such behavior in pnictides is not fully clarified, though for the $\text{LaFeAsO}_{1-x}\text{F}_x$ films it was explained as being due to an interplay of the BCS-gap optical feature and an absorption mode situated at frequencies just slightly above the gap [41]. A similar, but even more counterintuitive T dependence of the apparent optical gap was reported in MgB_2 [42]: there the minimum in $\sigma_1(\omega)$ decreased as $T \rightarrow 0$. This behavior was explained by the multiband nature of MgB_2 : the smaller gap dominates the optical response at the lowest temperature and the higher-frequency feature due to the larger gap is not well pronounced in the conductivity spectra. As T increases, the transition across the smaller gap becomes thermally saturated and the conductivity minimum gradually shifts to higher frequencies, revealing the optical feature related to the larger gap [42]. It seems plausible that multiband effects also affect the tem-

perature dependence of the optical gaps in pnictides.

The first observation of a superconducting energy gap in the reentrant phase enables us to go one step further, as it provides important information on the intermediate phase. The condensate forms right below $T_{c,\text{on}}$, although the density of superconducting electrons is very low. Since there is no superconducting path formed through the sample, the dc resistivity is not zero. Only below $T_{c,0} = 9.1$ K, when phase coherence is fully reached, $\rho(T)$ vanishes and a gap opens in the narrow conductivity term.

Our observations might be explained by scattering processes. Defects created by irradiation are known to quickly close the small superconducting gap with only minor effect on T_c [43]. Contrary to that Li *et al.* [44] suggested that in case of s_{\pm} symmetry, magnetic impurities act as interband scatterers, which hardly affect the transition temperature and do not break Cooper pairs. However, intraband magnetic scattering leads to pair breaking [44]. Accordingly, superconductivity is not destroyed as long as $1/\tau_{\text{inter}} > 1/\tau_{\text{intra}}$. We suggest that the different Eu^{2+} transitions lead to dominant intraband scattering at high T , but favor interband scattering in the superconducting phase at low temperatures. When $T_c \approx T_N$, Cooper pairs begin to condense, as evident in optics, but intraband magnetic scattering destroys the phase coherence causing a finite resistivity. When the spin-glass transition sets in, interband magnetic scattering prevails, permitting phase coherence and a fully developed superconducting state. Obviously the resistivity does not vanish immediately at the spin-glass transition; this can be simply explained by the inherent nature of a glass-like transition, which develops smoothly over a certain temperature range and does not appear abruptly.

While for the intermediate regime the presented scenario seems to be the most likely explanation of our findings, we recall that an increase in the low-frequency conductivity $\sigma_1(\omega)$ was previously taken as indication of pseudogap formation in iron-based superconductors [45]. Moreover, in cuprates the crossover between pseudogap and superconducting gap is known to take place at similar energy scale. Since we are very close to the limit of our resolvable measurement range, we cannot rule out that our observations are caused by a pseudogap-like formation, where the complex interaction of different magnetic transitions have an impact on the condensate of the Cooper pairs.

V. MAGNETIC PROPERTIES

In the parent compound EuFe_2As_2 , the Eu^{2+} magnetic moments order below $T_N = 19$ K in an A -type antiferromagnetic structure; i.e. while the spins are aligned ferromagnetically within the ab -plane, neighboring layers are coupled antiferromagnetically [46]. For $\text{EuFe}(\text{As}_{1-x}\text{P}_x)_2$, the isovalent substitution of As with P leads to a canting of the spins out of the ab -plane, and therefore to a

ferromagnetic net component along the c -direction [13]. As the canting increases with further P substitution, also the competition between ferromagnetism and antiferromagnetic Ruderman-Kittel-Kasuya-Yoshida (RKKY) exchange increases. Therefore, an additional magnetic phase – the reentrant spin glass phase – sets in at a certain amount of phosphorous with $T_{SG} < T_N$ [14]. As this phase might be the key in understanding how superconductivity coexists with the local magnetism in Eu-based iron pnictides, we carried out extensive magnetic investigations on our electron-doped EuFe_2As_2 compounds, $\text{Eu}(\text{Fe}_{0.91}\text{Ir}_{0.09})_2\text{As}_2$ and $\text{Eu}(\text{Fe}_{0.93}\text{Rh}_{0.07})_2\text{As}_2$.

A. Evidence for a spin glass

The most prominent feature identifying a spin-glass phase is the time dependence of the dc magnetization, together with a distinct frequency dependence of the ac-susceptibility known as Vogel-Fulcher behavior [47]. However, in superconductors also vortex dynamics leads to a time-dependent magnetization, hence complicating the analysis [48]. Nevertheless, as demonstrated previously for $\text{EuFe}(\text{As}_{1-x}\text{P}_x)_2$ [14], both phases can be separated by their opposite signs in the time-dependent behavior (for instance in the FCH-FCC curve, the difference between field-cooled heating and field-cooled cooling curves). Following the procedure developed for the isovalent substitution, in the following we will provide evidence that these phases are present in electron-doped samples, too.

1. $\text{Eu}(\text{Fe}_{0.91}\text{Ir}_{0.09})_2\text{As}_2$

For the Ir-doped sample, the characteristic magnetization data are presented in Fig. 7. The dc susceptibility [panel (a)] looks quite similar to the one obtained in Ref. 14: the double hump-like feature in the ZFC and FCH curve already indicates both magnetic transitions: the Eu-ordering corresponding to the first hump at $T_1 = T_N = 17.5$ K, and the spin-glass phase indicated by the second hump at $T_2 = T_{SG} = 15.9$ K, with $T_2 < T_1$. The measurements are performed at very low magnetic field ($\mu_0 H = 2$ G) since the spin-glass phase is already suppressed by 500 G.

Both, a thermal hysteresis (evidenced by the finite difference between field-cooled heating and zero-field cooled cooling curves: FCC-ZFC), and time-dependent processes (visible in $\text{FCH-FCC} \neq 0$) set in at the superconducting transition, which can be ascribed to vortex dynamics. At T_1 , a peak occurs in the FCH-FCC curve, and a dip in FCC-ZFC, meaning that the onset of Eu ordering influences the superconducting phase. At lower T , both differential curves show a sign change, which is typical for the spin-glass phase [14]. For the FCH-FCC curve, the sign change is not directly at T_2 , but at slightly lower temperatures, probably due to the dominant super-

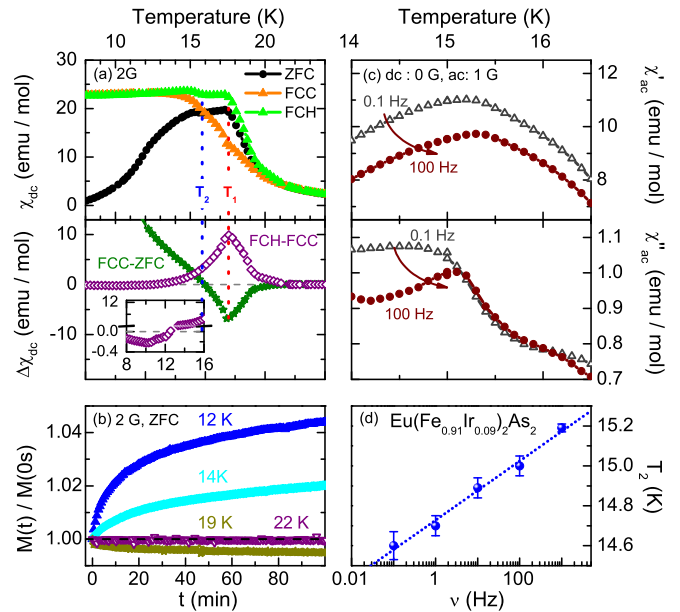


FIG. 7. (a-b) ab -plane dc and (c-d) ac-susceptibility of $\text{Eu}(\text{Fe}_{0.91}\text{Ir}_{0.09})_2\text{As}_2$ as a function of temperature. (a) While the upper frame shows the ZFC, FCC, and the FCH run, the lower one highlights the difference of the cooling and heating cycles. Thermal hysteresis is evidenced by a finite FCC-ZFC, while a non-zero value of FCH-FCC denotes time-dependent behavior. The temperatures T_1 and T_2 marked by the dotted lines correspond to two magnetic transitions. (b) Time-dependent measurements reveal two processes with opposite time-dependence. Below T_c , the magnetization decreases with time; at low temperatures, it increases. (c) Below T_2 , ac magnetic measurements show a frequency dependence in $\chi'_{ac}(T)$ and $\chi''_{ac}(T)$. (d) The peak position in $\chi''_{ac}(T)$ can be well described by a Vogel-Fulcher fit.

conducting state which masks the negative contribution. Time dependent measurements in the ZFC run further prove two distinct contributions to the overall time dependence as plotted in Fig. 7(b). It is important to note that any time dependence disappears at $T > T_c$, ruling out possible measurement artifact. For $T < T_c$ the normalized magnetization decreases with time, while for temperatures $T < T_2$, $M(t)$ increases significantly; we ascribe the stronger positive contribution to the spin-glass phase. Finally, the typical spin glass behavior can also be identified in ac susceptibility measurements with a very small amplitude of 1 G and without dc offset: here, a peak appears directly below T_2 in $\chi'_{ac}(T)$ and $\chi''_{ac}(T)$ [cf. Fig. 7(c)]. With increasing frequency, the peak shifts to higher temperatures. The peak position in χ''_{ac} follows a Vogel-Fulcher behavior, verifying the identification of this transition to the spin glass phase.

In the following we will discuss in more detail the imaginary part of the ac susceptibility, because it contains several different contributions, as best seen in a comparison between ac-, dc susceptibility and resistivity data [Fig. 8(a) and (b)]. The onset of superconductivity below $T < T_{c,on} \approx 21$ K leads to non-zero values in $\chi''_{ac}(T)$,

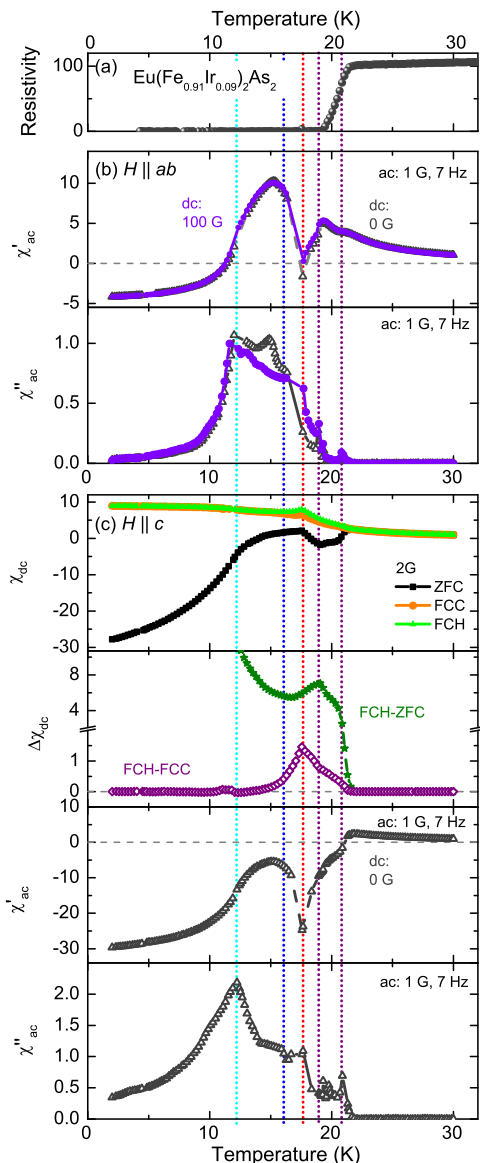


FIG. 8. (a) Resistivity and (b-c) magnetization of $\text{Eu}(\text{Fe}_{0.91}\text{Ir}_{0.09})_2\text{As}_2$ as a function of temperature (in emu/mol); the dotted lines are guides to the eye and mark the different transitions: in addition to the temperatures T_1 (red) and T_2 (blue), we also marked the response of the superconducting transition (purple) and another feature (cyan) not assigned yet. (a) The entrance to the superconducting state is clearly visible in the resistivity. (b) In-plane (ab) susceptibility data $\chi'_{ac}(T)$ (top) and $\chi''_{ac}(T)$ (bottom) for a dc offset of $\mu_0 H = 0$ G (grey) and 100 G (purple). $\chi''_{ac}(T)$ shows a wide variety of features: with decreasing temperature, a non-zero contribution develops below $T_{c,on}$ with a peak at approximately 21 K; a second peak denotes $T_{c,0} = 18.9$ K (purple). At $T_1 = 17.5$ K a minimum in $\chi'_{ac}(T)$ and a slope change in χ''_{ac} represents the antiferromagnetic transition (T_1 , red). Below $T_2 = 15.9$ K, a further peak develops in both contributions due to the spin-glass transition (T_2 , blue). (c) Measurements with $H \parallel c$ basically reveal the same transitions, however, there is no clear sign of the spin-glass transition. At $T = 12$ K a distinct peak in $\chi''_{ac}(T)$ and a slope change in $\chi'_{ac}(T)$ marks a possible unknown phase (cyan).

corresponding to the ZFC-FCH splitting due to screening currents in the dc magnetization [Fig. 7(a)]. A narrow sharp peak in $\chi''_{ac}(T)$ and a small dip in $\chi'_{ac}(T)$ at $T_{c,0}$ are caused by a maximum in the critical current density, known as peak effect [50]. Around $T_1 = 17.5$ K, a minimum in $\chi'_{ac}(T)$ coincides with the first peak in the ZFC-curve, marking the Eu^{2+} antiferromagnetic transition; it results from a destruction of the superconducting state by the local Eu-magnetism. Below $T_2 = 15.9$ K, a peak in $\chi'_{ac}(T)$ and $\chi''_{ac}(T)$ can be ascribed to the spin-glass phase; it is almost suppressed by a dc magnetic offset of only 100 G.

Additional information can be extracted from Fig. 8(c) where the magnetization results are displayed for applied fields along the c -direction. The most prominent feature for this orientation is the strong negative values for the ZFC magnetization reached at low temperatures; this is well known to result from the anisotropy of iron pnictides [49]. In general, screening currents form in the superconducting plane when a magnetic field is applied along the perpendicular direction. In iron pnictides, the ab -plane shows much higher superfluid densities than along the c -direction. Therefore, screening currents can develop much more efficiently within the ab -plane, visible as a negative magnetization for $H \parallel c$. Otherwise, for $H \parallel c$ superconductivity manifests in a way very similar to the in-plane direction: a thermal hysteresis at $T < T_{c,on}$, a peak at $\chi''_{ac}(T_{c,0})$, and the peak effect is visible.

The spin-glass phase, in contrast, is barely visible along the c -direction; for instance, in the ZFC, FCC, and FCH curves, only one hump can be detected, which corresponds to the antiferromagnetic transition at T_1 . A small hump is visible in the ac measurements, however, without any resolvable time- or frequency-dependence; therefore we ascribe it to a measurement artifact due to non-perfect alignment of the sample within the SQUID. For temperatures $T < T_1$, the FCC and FCH curves are rather flat; this is typical for an A -type antiferromagnet when the out-of-plane direction is probed. A small increase of these curves at lower temperatures, as well as a weak peak at $\chi''_{ac}(T_1)$ probably results from canting of the Eu^{2+} moments along the c -direction; similar observations have been reported for P-substituted samples [13]. Unfortunately, in the superconducting specimen its contribution is too weak for a clear identification.

2. $\text{Eu}(\text{Fe}_{0.93}\text{Rh}_{0.07})_2\text{As}_2$

Figure 9 presents the results of the magnetization measurements for the Rh-doped sample. In this case, the sample mass was at the sensitivity limit of the SQUID leading to much noisier curves than for the Ir specimen. However, the main features are very similar, as we will discuss in the following. The onset of superconductivity is barely visible but leads to slightly non-zero, positive FCH-FCC values. A hump in $\chi_{dc}(T)$ at $T_1 = 16.6$ K

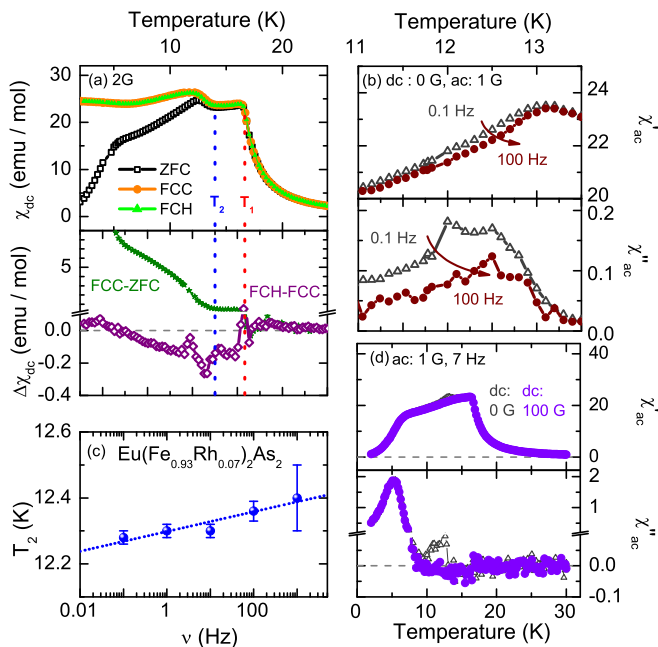


FIG. 9. (a) *ab*-plane static susceptibility and (b-d) ac susceptibility of $\text{Eu}(\text{Fe}_{0.93}\text{Rh}_{0.07})_2\text{As}_2$ plotted as a function of temperature (in emu/mol). (a) While the upper figure shows the ZFC, FCC and the FCH run, the lower one highlights the difference of the cooling and heating cycles. Thermal hysteresis is evidenced by a finite FCC-ZFC, while a non-zero value of FCH-FCC denotes time-dependent behavior. The temperatures T_1 and T_2 marked by the dotted lines correspond to two magnetic transitions. (b) Below T_2 , ac magnetic measurements show a frequency dependence in $\chi'_{ac}(T)$ and $\chi''_{ac}(T)$. (c) The peak position in $\chi''_{ac}(T)$ can be well described by a Vogel-Fulcher fit. (d) In-plane (*ab*) susceptibility data $\chi'_{ac}(T)$ (top) and $\chi''_{ac}(T)$ (bottom) for a dc offset of $\mu_0 H = 0$ G (grey) and 100 G (purple). For an offset field of 100 G the spin glass transition seems already fully suppressed.

marks the antiferromagnetic order; it corresponds to a weak peak in the FCH-FCC curve. At lower T the double hump-like feature in the ZFC, FCC and FCH curves, as well as negative values of FCH-FCC indicate the presence of the reentrant spin glass phase. In this case, as the superconducting state is weaker, the minimum of FCH-FCC appears much closer to T_2 than in the Ir sample. Again, the frequency-dependent ac susceptibility shows for increasing ac fields a shifting of the peaks in $\chi'_{ac}(T)$ and $\chi''_{ac}(T)$ to higher T , shown in Fig. 9(b); the peak position (fitted with a Gaussian distribution) also follows Vogel-Fulcher behavior as demonstrated in Fig. 9(c).

The poor signal-to-noise ratio does not allow us to extract here as much information from $\chi''_{ac}(T)$ as for $\text{Eu}(\text{Fe}_{0.91}\text{Ir}_{0.09})_2\text{As}_2$; nevertheless, for the sake of completeness, we present the results in Fig. 9(d) for a large temperature range. In contrast to the Ir-doped sample, for $\text{Eu}(\text{Fe}_{0.93}\text{Rh}_{0.07})_2\text{As}_2$ $\chi'_{ac}(T)$ does not reach negative values, indicating a stronger Eu^{2+} magnetism and/or a weaker superconductivity phase – which would be both consistent with speculations that this sample is actually

underdoped. For an offset of $\mu_0 H = 0$ G, a peak is located below T_2 in both, $\chi'_{ac}(T)$ and $\chi''_{ac}(T)$, corresponding to the spin-glass phase. For a constant magnetic-field offset of $\mu_0 H = 100$ G, it is already completely suppressed. Similar to the Ir sample, an additional pronounced peak appears in $\chi''_{ac}(T)$ at lower temperatures.

B. Indications for an additional magnetic transition

From our ac susceptibility measurements over a broad temperature range, we could identify a very pronounced peak in $\chi''_{ac}(T)$, which also appears as an inflection point in $\chi'_{ac}(T)$ and in the ZFC curve. This feature can be seen even better when the magnetic field is applied along the *c*-direction. While a dc-offset of $\mu_0 H = 100$ G completely suppresses the spin-glass peak in $\chi''_{ac}(T)$, this additional feature is barely affected by this offset. For $\text{Eu}(\text{Fe}_{0.91}\text{Ir}_{0.09})_2\text{As}_2$ the feature appears around 12 K; for the Rh-doped sample, at 5 K. There are two possibilities to explain the observation of this signal. A ferromagnetic canting or phase would lead to a signal in $\chi''_{ac}(T)$. In Ref. 3 an extensive discussion is presented why the canting of the moments does not take place directly at T_N , but develops with decreasing temperature. This would explain the observation of an additional phase in Ru-doped compounds [15]. Alternatively, the feature could originate due to complex vortex dynamics. In order to resolve this issue, further investigations on overdoped samples should be carried out, which do not show any traces of superconductivity.

VI. CONCLUSION

Transport and magnetic investigations on electron-doped $\text{Eu}(\text{Fe}_{0.91}\text{Ir}_{0.09})_2\text{As}_2$ and $\text{Eu}(\text{Fe}_{0.93}\text{Rh}_{0.07})_2\text{As}_2$ single crystals revealed the presence of the reentrant spin-glass phase. The properties resemble the behavior observed in isovalent substituted $\text{EuFe}_2(\text{As}_{1-x}\text{P}_x)_2$ compounds [14]. Since the two materials contain different dopants, we suggest that the reentrant spin-glass phase is present in all electron-doped compounds. For the Ir-doped sample, a very strong feature in the imaginary part of the ac susceptibility was found, which might be explained by vortex dynamics; however, future investigations on different doping levels are necessary to clarify its origin.

Optical measurements revealed that at low-frequencies the normal-state optical response of each compound is dominated by two Drude-like components with different scattering rates. At the lowest temperatures, in the superconducting state, the Drude components become gapped and the optical spectra can be best described by two full-gap dirty-limit BCS terms, with the gap values being close to each other for both the terms in each system. In $\text{Eu}(\text{Fe}_{0.93}\text{Rh}_{0.07})_2\text{As}_2$, the traces of reentrant superconductivity are seen in the optical spectra:

in the reentrant phase only one basically temperature-independent gap can be resolved, while a second superconducting gap gets merely visible at the lowest temperatures when zero-resistivity is finally reached. We explain this behavior as the effect of magnetism: the superconducting state can fully develop only when the spin-glass

phase is formed.

VII. ACKNOWLEDGMENT

We thank U. S. Pracht for fruitful discussions and G. Untereiner for expert experimental support. This work was supported by the Deutsche Forschungsgemeinschaft (DFG SPP 1458, DR228/42-1 and DR228/44-1).

-
- [1] Y. Kamihara, T. Watanabe, M. Hirano, and H. Hosono, *J. Am. Chem. Soc.* **130** (11), 3296 (2008).
- [2] N. L. Wang, H. Hosono, and P. Dai, *Iron-based Superconductors - Materials, Properties and Mechanisms*, (Pan Stanford Publishing Pte. Ltd., 2013).
- [3] S. Zapf, and M. Dressel, *Rep. Progr. Phys.* **80**, 016501 (2017).
- [4] D. Wu, N. Barišić, N. Drichko, S. Kaiser, A. Faridian, M. Dressel, S. Jiang, Z. Ren, L.-J. Li, G.-H. Cao, Z.-A. Xu, H.-S. Jeevan, and P. Gegenwart, *Phys. Rev. B* **79**, 155103 (2009).
- [5] S. Zapf, C. Stingl, K. W. Post, J. Maiwald, N. Bach, I. Pietsch, D. Neubauer, A. Löhle, C. Clauss, S. Jiang, H. S. Jeevan, D. N. Basov, P. Gegenwart, and M. Dressel, *Phys. Rev. Lett.* **113**, 227001 (2014).
- [6] E. Müller-Hartmann, and J. Zittartz, *Phys. Rev. Lett.* **26**, 428 (1971).
- [7] K.-H. Müller, and V. N. Narozhnyi, *Rep. Prog. Phys.* **64**, 943 (2001).
- [8] U. B. Paramanik, Debarchan Das, R. Prasad, and Z. Hossain, *J. Phys.: Condens. Matter* **25**, 26 (2013).
- [9] C. F. Miclea, M. Nicklas, H. S. Jeevan, D. Kasinathan, Z. Hossain, H. Rosner, P. Gegenwart, C. Geibel, and F. Steglich, *Phys. Rev. B* **79**, 212509 (2009).
- [10] W.-H. Jiao, Y. Liu, Z.-T. Tang, Y.-K. Li, X.-F. Xu, Z. Ren, Z.-A. Xu, and G.-H. Cao, *Supercond. Sci. Technol.* **30**, 025012 (2017).
- [11] S. Jiang, Y. K. Luo, Z. Ren, Z. W. Zhu, C. Wang, X. F. Xu, Q. Tao, G. H. Cao, and Z. A. Xu, *New J. Phys.* **11**, 025007 (2009).
- [12] W. H. Jiao, Q. Tao, J. K. Bao, Y. L. Sun, C. M. Feng, Z. A. Xu, I. Nowik, I. Felner, and G. H. Cao, *Europhys. Lett.* **95**, 67007 (2011).
- [13] S. Zapf, D. Wu, L. Bogani, H. S. Jeevan, P. Gegenwart, and M. Dressel, *Phys. Rev. B* **84**, 140503 (2011).
- [14] S. Zapf, H. S. Jeevan, T. Ivek, F. Pfister, F. Klingert, S. Jiang, D. Wu, P. Gegenwart, R. K. Kremer, and M. Dressel, *Phys. Rev. Lett.* **110**, 237002 (2013).
- [15] W. H. Jiao, J. K. Bao, Q. Tao, H. Jiang, C. M. Feng, Z. A. Xu, and G. H. Cao, *JPCS* **400**, 022038 (2012).
- [16] W. T. Jin, S. Nandi, Y. Xiao, Y. Su, O. Zaharko, Z. Guguchia, Z. Bukowski, S. Price, W. H. Jiao, G. H. Cao, and Th. Brückel, *Phys. Rev. B* **88**, 214516 (2013).
- [17] V. K. Anand, D. T. Adroja, A. Bhattacharyya, U. B. Paramanik, P. Manuel, A. D. Hillier, D. Khalyavin, and Z. Hossain, *Phys. Rev. B* **91**, 094427 (2015).
- [18] W. T. Jin, W. Li, Y. Su, S. Nandi, Y. Xiao, W. H. Jiao, M. Meven, A. P. Sazonov, E. Feng, Y. Chen, C. S. Ting, G. H. Cao, and Th. Brückel, *Phys. Rev. B* **91**, 064506 (2015).
- [19] S. Nandi, W. T. Jin, Y. Xiao, Y. Su, S. Price, D. K. Shukla, J. Strempfer, H. S. Jeevan, P. Gegenwart, and Th. Brückel, *Phys. Rev. B* **89**, 014512 (2014).
- [20] W. H. Jiao, H. F. Zhai, J. K. Bao, Y. K. Luo, Q. Tao, C. M. Feng, Z. A. Xu, and G. H. Cao, *New. J. Phys.* **15**, 113002 (2013).
- [21] T. Shibauchi, A. Carrington, and Y. Matsuda, *Ann. Rev. Condens. Matter Phys.* **5**, 113 (2014).
- [22] N. Kurita, M. Kimata, K. Kodama, A. Harada, M. Tomita, H.-S. Suzuki, T. Matsumoto, K. Murata, S. Uji, and T. Terashima, *Phys. Rev. B* **88**, 224510 (2013).
- [23] N. Barišić, D. Wu, M. Dressel, L. J. Li, G. H. Cao, and Z. A. Xu, *Phys. Rev. B* **82**, 054518 (2010).
- [24] Y. Tokiwa, S. H. Hübner, O. Beck, H. S. Jeevan, and P. Gegenwart, *Phys. Rev. B* **86**, 220505 (2012).
- [25] S. Zapf, D. Neubauer, K. W. Post, A. Kadau, J. Merz, C. Clauss, A. Löhle, H. S. Jeevan, P. Gegenwart, D. N. Basov, and M. Dressel, *Compt. Ren. Phys.* **17**, 188 (2016).
- [26] D. Wu, N. Barišić, P. Kallina, A. Faridian, B. Gorshunov, N. Drichko, L. J. Li, X. Lin, G. H. Cao, Z. A. Xu, N. L. Wang, and M. Dressel, *Phys. Rev. B* **81**, 100512 (2010).
- [27] M. Dressel and G. Grüner, *Electrodynamics of Solids* (Cambridge University Press, Cambridge, 2002).
- [28] M. Nakajima, T. Liang, S. Ishida, Y. Tomioka, K. Kihou, C. H. Lee, A. Iyo, H. Eisaki, T. Kakeshita, T. Ito, and S. Uchida, *Proc. Nat. Acad. Sci.* **108**, 12238 (2011).
- [29] X. Bing, D. Yao-Min, X. Hong, R. P. S. M. Lobo, and Q. Xiang-Gang, *Chinese Physics B* **23**, 087401 (2014).
- [30] A. A. Schafgans, S. J. Moon, B. C. Pursley, A. D. LaForge, M. M. Qazilbash, A. S. Sefat, D. Mandrus, K. Haule, G. Kotliar, and D. N. Basov, *Phys. Rev. Lett.* **108**, 147002 (2012).
- [31] V.I. Torgashev, private communications (2009).
- [32] A. Akrap, J. J. Tu, L. J. Li, G. H. Cao, Z. A. Xu, and C. C. Homes, *Phys. Rev. B* **80**, 180502 (2009).
- [33] M. Dressel, *Adv. Condens. Matter Phys.* **2013**, 104379, (2013).
- [34] U. S. Pracht, E. Heintze, C. Clauss, D. Hafner, R. Bek, D. Werner, S. Gelhorn, M. Scheffler, M. Dressel, D. Sherman, B. Gorshunov, K. S. Ilin, D. Henrich, M. Siegel *IEEE Trans. THz Sci. Technol.* **3**, 269 (2013).
- [35] E. G. Maksimov, A. E. Karakozov, B. P. Gorshunov, A.S. Prokhorov, A. A. Voronkov, E. S. Zhukova, V. S. Nozdrin, S. S. Zhukov, D. Wu, M. Dressel, S. Haindl, K. Iida, and B. Holzapfel, *Phys. Rev. B* **83**, 140502 (2011).
- [36] M. Dressel, D. Wu, N. Barišić, and B. P. Gorshunov, *J. Phys. Chem. Solids* **72**, 514 (2011).

- [37] D. Neubauer, A. V. Pronin, S. Zapf, J. Merz, H. S. Jeevan, W. H. Jiao, P. Gegenwart, G. H. Cao and M. Dressel, *Phys. Stat. Sol. B*, **254**, 1600148 (2017).
- [38] Y. M. Dai, H. Miao, L. Y. Xing, X. C. Wang, C. Q. Jin, H. Ding, and C. C. Homes, *Phys. Rev. B* **93**, 054508 (2016).
- [39] We should note that it might not be appropriate to identify the narrow and broad Drude components with different bands. Also the clean and dirty limit superconductivity in $\text{Eu}(\text{Fe}_{0.91}\text{Ir}_{0.09})_2\text{As}_2$, $\text{Eu}(\text{Fe}_{0.93}\text{Rh}_{0.07})_2\text{As}_2$ and possibly in other pnictides should not simply be assigned to distinct bands as intra- and interband scattering processes might be of importance.
- [40] R. P. S. M. Lobo, Y. M. Dai, U. Nagel, T. R  m, J. P. Carbotte, T. Timusk, A. Forget, and D. Colson, *Phys. Rev. B* **82**, 100506 (2010).
- [41] X. Xi, Y. M. Dai, C. C. Homes, M. Kizun, S. Haindl, and G. L. Carr, *Phys. Rev. B* **87**, 180509 (2013).
- [42] A. Pimenov, A. Loidl, and S. I. Krasnovobodtsev, *Phys. Rev. B* **65**, 172502 (2002).
- [43] M. B. Schilling, A. Baumgartner, B. Gorshunov, E.S Zhukova, V.A. Dravin, K.V. Mitsen, D. V. Efremov, O. V. Dolgov, K. Iida, M. Dressel, and S. Zapf, *Phys. Rev. B* **93**, 174515 (2016).
- [44] J. Li, and Y. Wang, *EPL (Europhys. Lett.)* **88**, 17009 (2009).
- [45] S. J. Moon, A. A. Schafgans, S. Kasahara, T. Shibauchi, T. Terashima, Y. Matsuda, M. A. Tanatar, R. Prozorov, A. Thaler, P. C. Canfield, A. S. Sefat, D. Mandrus, and D. N. Basov, *Phys. Rev. Lett.* **109**, 027006 (2012).
- [46] S. Jiang, Y. Luo, Z. Ren, Z. Zhu, C. Wang, X. Xu, Q. Tao, G. Cao, and Z. Xu, *New J. Phys.* **11**, 025007 (2009).
- [47] K. Binder, and A. P. Young, *Rev. Mod. Phys.* **58**, 801 (1986).
- [48] W. Zhou, X. Xing, W. Wu, H. Zhao, and Z. Shi, *Sci. Rep.* **6**, 22278 (2016).
- [49] S. J. Moon, A. A. Schafgans, M. A. Tanatar, R. Prozorov, A. Thaler, P. C. Canfield, A. S. Sefat, D. Mandrus, and D. N. Basov, *Phys. Rev. Lett.* **110**, 097003 (2013).
- [50] J. Giapintzakis, R. L. Neiman, D. M. Ginsberg, and M. A. Kirk, *Phys. Rev. B* **50**, 16001 (1994).